



# Texas Spectroscopic Search for Ly $\alpha$ Emission at the End of Reionization. II. The Deepest Near-infrared Spectroscopic Observation at $z \gtrsim 7$

Intae Jung<sup>1</sup>, Steven L. Finkelstein<sup>1</sup>, Mark Dickinson<sup>2</sup>, Taylor A. Hutchison<sup>3,4</sup>, Rebecca L. Larson<sup>1</sup>, Casey Papovich<sup>3,4</sup>, Laura Pentericci<sup>5</sup>, Mimi Song<sup>6</sup>, Henry C. Ferguson<sup>7</sup>, Yicheng Guo<sup>8</sup>, Sangeeta Malhotra<sup>6,9</sup>, Bahram Mobasher<sup>10</sup>,

James Rhoads<sup>6,9</sup>, Vithal Tilvi<sup>9</sup>, and Isak Wold<sup>6</sup>

<sup>1</sup> Department of Astronomy, The University of Texas at Austin, Austin, TX 78712, USA; [itjung@astro.as.utexas.edu](mailto:itjung@astro.as.utexas.edu)

<sup>2</sup> National Optical Astronomy Observatory, Tucson, AZ 85719, USA

<sup>3</sup> Department of Physics and Astronomy, Texas A&M University, College Station, TX 77843-4242, USA

<sup>4</sup> George P. and Cynthia Woods Mitchell Institute for Fundamental Physics and Astronomy, Texas A&M University, College Station, TX 77843-4242, USA

<sup>5</sup> INAF, Osservatorio Astronomico di Roma, via Frascati 33, I-00078, Monteporzio Catone, Italy

<sup>6</sup> Astrophysics Science Division, Goddard Space Flight Center, Greenbelt, MD 20771, USA

<sup>7</sup> Space Telescope Science Institute, 3700 San Martin Drive, Baltimore, MD 21218, USA

<sup>8</sup> Department of Physics and Astronomy, University of Missouri, Columbia, MO, USA

<sup>9</sup> School of Earth & Space Exploration, Arizona State University, Tempe, AZ 85287, USA

<sup>10</sup> Department of Physics and Astronomy, University of California, Riverside, CA 92521, USA

Received 2019 January 16; revised 2019 April 15; accepted 2019 April 22; published 2019 June 5

## Abstract

Realizing the utility of Ly $\alpha$  emission to trace the evolution of the intergalactic medium (IGM) during the epoch of reionization requires deep spectroscopy across the boundary of optical and near-infrared (NIR) spectrographs at  $z \sim 7.2$  when Ly $\alpha$  emission is at  $\sim 1 \mu\text{m}$ . Our Texas Spectroscopic Search for Ly $\alpha$  Emission at the End of Reionization includes 18 nights of deep spectroscopic observations using the Keck DEIMOS (optical) and MOSFIRE (NIR) spectrographs. Within this data set we observe Ly $\alpha$  emission from 183 photometric-redshift-selected galaxies at  $z = 5.5$ –8.3 from the Cosmic Assembly Near infrared Deep Extragalactic Legacy Survey. Our overlapping MOSFIRE observations, over 84 galaxies in total, provide the deepest NIR spectroscopic data yet obtained for Ly $\alpha$  from galaxies  $z > 7$ , with  $>16$  hr integration time for four observed galaxies. Here we analyze these four targets, and we report the discovery of a new  $z = 7.60$  Ly $\alpha$  detection as well as provide an updated observation of the previously confirmed  $z = 7.51$  Ly $\alpha$  emission from Finkelstein et al. with a  $\sim 3 \times$  longer exposure time. Our analysis of these Ly $\alpha$  emission-line profiles reveals a significant asymmetric shape. The detection of Ly $\alpha$  from two out of three bright sources ( $M_{\text{UV}} < -20.25$ ) could imply that these bright galaxies inhabit ionized bubbles in a partially neutral IGM, although deeper exposures may reveal Ly $\alpha$  emission in the fainter source.

**Key words:** early universe – galaxies: distances and redshifts – galaxies: evolution – galaxies: formation – galaxies: high-redshift – intergalactic medium

## 1. Introduction

Charting the timeline of reionization through useful tracers such as Ly $\alpha$  forest absorption in high- $z$  quasars (e.g., Becker et al. 2001; Fan et al. 2006; Bolton et al. 2011; Mortlock et al. 2011; McGreer et al. 2015; Bosman et al. 2018), the cosmic microwave background polarization measurement (Larson et al. 2011; Planck Collaboration et al. 2016), and Ly $\alpha$  emitter (LAE) observations (e.g., Miralda-Escudé & Rees 1998; Rhoads & Malhotra 2001; Malhotra & Rhoads 2004) constrains how galaxies and the intergalactic medium (IGM) interplay in the early universe. As the dominant sources of the ionizing photons are thought to be galaxies (e.g., Finkelstein et al. 2015; Robertson et al. 2015), investigating the evolution of the IGM during reionization provides critical constraints on the evolution of distant galaxies in the early universe, as well as the impact of the IGM on the formation and evolution of galaxies at that epoch.

Ly $\alpha$  emission has emerged as a useful tracer of the evolution of the IGM near the end of reionization (e.g., Becker et al. 2018), as Ly $\alpha$  emission is easily diminished with even small amounts of neutral hydrogen due to the resonant nature of Ly $\alpha$  scattering with neutral hydrogen (e.g., Rybicki & Loeb 1999; Santos 2004; Dayal et al. 2011; Dijkstra 2014). For instance,

narrowband Ly $\alpha$  surveys provide a statistical number of Ly $\alpha$  emitters (LAEs) for Ly $\alpha$  luminosity functions (LFs), and the evolution of the Ly $\alpha$  LF at  $z \gtrsim 6$  suggests an increasing fraction of neutral hydrogen in the IGM (e.g., Hu et al. 2010; Ouchi et al. 2010; Kashikawa et al. 2011; Zheng et al. 2017; Konno et al. 2018). From follow-up spectroscopic observations for high- $z$  candidate galaxies or Lyman-break galaxies, a simple measure of the Ly $\alpha$  fraction, which is the number of Ly $\alpha$  emitters among the number of spectroscopically observed candidates, shows an apparent deficit of Ly $\alpha$  emission at  $z > 6.5$ . The drop in Ly $\alpha$  emission at  $z > 6$  implies that the H I fraction in the IGM increases significantly from  $z \sim 6 \rightarrow 7$  (e.g., Fontana et al. 2010; Stark et al. 2010; Pentericci et al. 2011, 2014; Caruana et al. 2012, 2014; Curtis-Lake et al. 2012; Mallery et al. 2012; Ono et al. 2012; Schenker et al. 2012, 2014; Treu et al. 2012, 2013; Tilvi et al. 2014; Vanzella et al. 2014; Schmidt et al. 2016).

Recently, with extensive Ly $\alpha$  spectroscopic data of  $\gtrsim 60$  Ly $\alpha$  detected galaxies at  $z \sim 6$ –7, Pentericci et al. (2018) suggested a smoother evolution of the IGM with their measurement of the Ly $\alpha$  fraction at  $z \sim 6$ –7, where they found little evolution from  $z \sim 5 \rightarrow 6$  and a larger drop from  $z \sim 6 \rightarrow 7$ . This reveals that the IGM was not fully ionized by  $z = 6$ , thus a smaller evolution in the neutral fraction from

$z = 6$  to 7 is needed to explain the observations. An analogous analysis of the Ly $\alpha$  fraction becomes very challenging at  $z > 7$ . Although spectroscopic follow-up observations with ground-based telescopes and the *Hubble Space Telescope* (*HST*) grism have been successful in searching for Ly $\alpha$  emission at  $z \sim 7$  (e.g., Fontana et al. 2010; Shibuya et al. 2012; Pentericci et al. 2014; Larson et al. 2018), only six Ly $\alpha$  emitting galaxies have been detected at greater than the  $5\sigma$  level so far at  $z > 7.5$  (Finkelstein et al. 2013; Oesch et al. 2015; Zitrin et al. 2015; Song et al. 2016; Hoag et al. 2017; Laporte et al. 2017). These non-detections may imply a further drop in the IGM neutral fraction, but this interpretation is non-trivial given the limited spectroscopic depths of most previous near-infrared (NIR) spectroscopic observations, and the uncertainty in the expected line wavelength due to the uncertainty of photometric redshift measurements.

In our first paper in this series (Jung et al. 2018) from our *Texas Spectroscopic Search for Ly $\alpha$  Emission at the End of Reionization*, we introduced our methodology for constraining the evolution of the Ly $\alpha$  EW distribution accounting for all observational incompleteness effects (e.g., photometric redshift probability distribution function, UV continuum luminosity, instrumental wavelength coverage, and observing depth). We found evidence that the Ly $\alpha$  EW distribution evolves to lower values at  $z > 6$ , suggesting an increasing neutral hydrogen fraction in the IGM. To move to  $z > 7$  we require NIR spectroscopy.

We obtained deep NIR spectroscopic data with Keck/MOSFIRE over 84 candidate galaxies. Because these observations partially overlapped on the sky, we achieved  $\gtrsim 16$  hr integration time for four high- $z$  candidate galaxies at  $z \gtrsim 7$ . In this paper, we present the results from these ultra-deep NIR spectroscopic observations with MOSFIRE for four  $z \gtrsim 7$  galaxies, reporting a new Ly $\alpha$  emission line at  $z = 7.60$  as well as the updated measurement of the previously reported  $z = 7.51$  Ly $\alpha$  emitter (Finkelstein et al. 2013) with a  $\sim 3 \times$  longer exposure time. We describe our MOSFIRE data set and data reduction procedures in Section 2, and report the detected Ly $\alpha$  emission lines at  $z > 7$  in Section 3. Section 4 summarizes our findings with our deepest NIR observations and discusses the Ly $\alpha$  visibility. In this work, we assume the *Planck* cosmology (Planck Collaboration et al. 2016) with  $H_0 = 67.8 \text{ km s}^{-1} \text{ Mpc}^{-1}$ ,  $\Omega_M = 0.308$  and  $\Omega_\Lambda = 0.692$ . The *HST* F435W, F606W, F775W, F814W, F850LP, F105W, F125W, F140W, and F160W bands are referred as  $B_{435}$ ,  $V_{606}$ ,  $i_{775}$ ,  $I_{814}$ ,  $z_{850}$ ,  $Y_{105}$ ,  $J_{125}$ ,  $JH_{140}$ , and  $H_{160}$ , respectively. All magnitudes are given in the AB system (Oke & Gunn 1983), and all errors presented in this paper represent  $1\sigma$  uncertainties (or central 68% confidence ranges), unless stated otherwise.

## 2. Data

### 2.1. Texas Spectroscopic Search for Ly $\alpha$ Emission at the End of Reionization

To search for Ly $\alpha$  emission from galaxies in the reionization era, we performed deep spectroscopic observations of candidate galaxies in the GOODS-S and GOODS-N fields from the Cosmic Assembly Near-infrared Deep Extragalactic Legacy Survey (CANDELS; PIs Faber & Ferguson). This consists of a total of 18 nights of spectroscopic observations targeting 183 galaxies at  $z > 5$ : for 118 galaxies with Keck/DEIMOS (PI: R. Livermore) and 84 galaxies with Keck/MOSFIRE (PI: S.

Finkelstein; the majority coming through the NASA/Keck allocation). The entire program is described in Jung et al. (2018) where we discuss our measure of the Ly $\alpha$  EW distribution at  $z \sim 6.5$  with DEIMOS. The target galaxies were selected from the Finkelstein et al. (2013, 2015) photometric catalogs. The selection criteria for our masks prioritizes galaxy brightness and the photometric redshift probability being within the  $Y$ -band instrumental wavelength coverage to maximize the chance of detecting Ly $\alpha$  emission. We utilize MAGMA, the public MOSFIRE slit-mask design tool,<sup>11</sup> which automatically generates slit-mask designs based on prioritized target lists. The entire observation program was performed through multiple nights with different slit-mask configurations. With this observing strategy, a portion of targets were observed in multiple masks, which ended up having four targets with the longest exposure over 16 hr. In this paper we report a new Ly $\alpha$  emission line at  $z = 7.60$ , analyzing our deepest MOSFIRE observations for four  $z \gtrsim 7$  galaxies. The Ly $\alpha$  EW distribution analysis using our entire MOSFIRE data set will be discussed in a future publication.

### 2.2. MOSFIRE Y-band Observations in GOODS-N

Our GOODS-N MOSFIRE data set was obtained through 10 nights of observations with 6 different mask designs from 2013 April to 2015 February, targeting 72 galaxies at  $z \gtrsim 6$ . Table 1 summarizes our Keck/MOSFIRE observations in GOODS-N. In this paper we present the results from our deepest MOSFIRE data set for the four candidate galaxies, which are summarized in Table 2. We used the  $Y$ -band filter with a  $0.^{\prime\prime}7$  slit width and a spectral resolution of  $\sim 3 \text{ \AA}$  ( $R = 3500$ ), covering Ly $\alpha$  over a redshift range of  $7.0 < z < 8.2$ . In our observations, we take 180 s exposures in individual frames with an ABAB dither pattern ( $+1.^{\prime\prime}25, -1.^{\prime\prime}25, +1.^{\prime\prime}25, -1.^{\prime\prime}25$ ), thus the positions in the adjacent frames are separated by  $2.^{\prime\prime}5$ .

We note that our GOODS-N MOSFIRE program included six objects with  $> 16$  hr integration time, which were classified as high- $z$  candidates from Finkelstein et al. (2013, 2015). However, two of the six candidates now appear to more likely be low- $z$  galaxies from an updated photometric redshift measurement including deep  $I_{814}$  and *Spitzer*/IRAC photometry (S. Finkelstein et al. 2019, in preparation), which were not included in the Finkelstein et al. (2013, 2015) measurements. With the updated photometry and the photometric redshifts, we update the measure of  $M_{UV}$  of our target galaxies as well, which are derived via spectral energy distribution (SED) fitting. We note these two likely low- $z$  galaxies show no significant features in their spectra. We thus focus this paper on the remaining four targets. Each of the four targets was observed in three of the MOSFIRE masks, resulting in the longest NIR spectroscopic follow-up observation for Ly $\alpha$  at  $z \gtrsim 7$ , with a total exposure of  $> 16$  hr.

### 2.3. Data Reduction

The data were reduced using Version 2018 of the public MOSFIRE data reduction pipeline (DRP),<sup>12</sup> which provides a sky-subtracted, flat-fielded, and rectified two-dimensional (2D) slit spectrum per object with a wavelength solution using telluric sky emission lines. The reduced 2D spectra have a

<sup>11</sup> <https://www2.keck.hawaii.edu/inst/mosfire/magma.html>

<sup>12</sup> <http://keck-datalreductionpipelines.github.io/MosfireDRP/>

**Table 1**  
Summary of Keck/MOSFIRE Observations in GOODS-N

Mask Name	R.A. (J2000.0)	Decl. (J2000.0)	Observation Dates	$N_{\text{targets}}$	$t_{\text{exp}}$ (hr)	Seeing <sup>a</sup> (arcsec)	Standard Star <sup>b</sup>
GOODSN_Mask1	189.162917	62.274244	2013 Apr 18	24	5.8	0.7	HIP56147
GOODSN_Mask2	189.312875	62.279597	2013 Apr 19	19	5.5	0.6	HIP56147
GOODSN_Y_v12	189.244875	62.274253	2014 Mar 14, 15, 25	23	6.3	0.9	HIP53735, HIP65280
gdn1404_Y1_3	189.339667	62.324689	2014 Apr 17, 18, May 13	13	7.2	1.3	HIP65280
Mask2_Y_2015A	189.214083	62.265297	2015 Feb 23, 24	10	4.5	0.8	HIP56147
Mask1_Y_2015A_2	189.331125	62.204139	2015 Feb 23, 24	10	4.5	1.2	HIP56147

**Notes.**<sup>a</sup> FWHM measured from continuum objects in mask configurations.<sup>b</sup> The flux calibration standard stars in our long-slit observations, listed in the *Hipparcos* index (van Leeuwen 2007).

**Table 2**  
Summary of Four Targets with  $t_{\text{exp}} > 16$  hr

ID <sup>a</sup>	R.A. (J2000.0)	Decl. (J2000.0)	$t_{\text{exp}}$ (hr)	$M_{\text{UV}}^{\text{b}}$	$z_{\text{phot}}$	$z_{\text{spec}}^{\text{c}}$	$\text{EW}_{\text{Ly}\alpha}^{\text{d}}$ (Å)
z7_GND_18869	189.205292	62.250767	16.5	-20.43	$6.96^{+0.02}_{-0.05}$	...	<19.90
z7_GND_16863	189.333083	62.257236	16.3	-21.24	$7.21^{+0.13}_{-0.13}$	7.60	$61.28 \pm 5.85$
z7_GND_42912 <sup>e</sup>	189.157875	62.302372	16.5	-21.58	$7.43^{+0.11}_{-0.12}$	7.51	$33.19 \pm 3.20$
z8_GND_9408	189.300125	62.280358	19.0	-19.70	$7.41^{+0.44}_{-7.18}$	...	<65.58

**Notes.**<sup>a</sup> The listed IDs are from Finkelstein et al. (2015), encoded with their photometric redshifts and the fields in the CANDELS imaging data.<sup>b</sup>  $M_{\text{UV}}$  is the averaged magnitude at 1500 Å, derived from galaxy SED fitting with stellar population synthesis models.<sup>c</sup> The  $z_{\text{spec}}$  measurement errors are  $\lesssim 0.001$ .<sup>d</sup>  $5\sigma$  upper limits for non-detections.<sup>e</sup> Known as z8\_GND\_5296 in Finkelstein et al. (2013).

spectral resolution of  $1.09 \text{ \AA pixel}^{-1}$  and a spatial resolution of  $0.^{\prime\prime}18 \text{ pixel}^{-1}$ . However, pre-2017 MOSFIRE observations were subject to a noticeable drift of object spectra in the spatial direction along the slit, thought to be due to differential atmospheric refraction (e.g., Kriek et al. 2015; Song et al. 2016). We detected systematic slit drifts (up to  $\sim 1 \text{ pixel hr}^{-1}$ ) in all observations, with a noticeable dependence on airmass. To correct for this drifting of object spectra, we ran the MOSFIRE DRP on each adjacent pair of images, and measured the relative slit drift by marking the position of the spectrum of a star we put on one of our slits. Correcting for the derived slit drifts, we combined individual DRP outputs to generate all combined 2D spectra. In the combination step, we rejected any bad pixel or cosmic rays by taking sigma-clipped means, and we measured the best-fit Gaussian peak fluxes of the continuum sources as the weight factors of the DRP outputs.

Flux calibration and telluric absorption correction were done on individual nights, using long-slit observations of a spectro-photometric standard star (listed in Table 1) and the model stellar spectrum of Kurucz (1993). The response curve is obtained by dividing the model stellar spectra (scaled to have the known broadband magnitudes of the standard stars) with the observed spectra from the long-slit observations. In the case where each mask was observed on multiple nights, we combined all 2D spectra, which were individually calibrated, to generate a single 2D spectrum per mask design. We validated our calibration using the known  $Y_{105}$  magnitudes of continuum objects in the mask configurations (the magnitudes are from the updated photometric catalog of S. Finkelstein et al. 2019, in preparation). As these objects were observed contemporaneously with our science

objects, they were observed under identical conditions, compared to the standard stars which may not have been. We therefore used these objects to calculate and apply a residual normalization correction to our flux calibration array, as the ratio of the known  $Y$ -band magnitudes of the slit continuum objects to those from the calibrated spectra, typically up to a  $\sim 30\%-50\%$  effect.

In slit spectroscopic observations for unresolved sources, it is generally recommended that the slit width match the seeing level. This is because a larger choice of the slit width decreases a spectral resolution and increases a sky background (refer Chapter 4.4.1 in Appenzeller 2013). Therefore, we were motivated to choose a slit width of  $0.^{\prime\prime}7$  for the typical seeing level of Maunakea ( $\sim 0.^{\prime\prime}7$ ), although less favorable observing conditions on nights with seeing  $> 0.^{\prime\prime}7$  might have an impact on our Ly $\alpha$  detection rate. Our flux calibration procedure, which includes a correction based on the stars on our mask, also includes a treatment to correct for these slit losses, assuming our high-redshift candidate galaxies are point sources, as they are unresolved in our observations.

The four targets with the longest exposure were observed in three different mask configurations. Thus, after combining all individual mask spectra, weighted by median-noise levels, we obtained fully reduced, all-mask-combined, and flux-calibrated 2D spectra for the targets. To extract one-dimensional (1D) spectra, we performed an optimal extraction (Horne 1986) with a  $2.^{\prime\prime}5$  spatial aperture. The optimal extraction uses a spatial weighting from the stellar profile. Therefore, the bulk of the weighting is within the FWHM of the star, i.e., the seeing, and thus is  $< 1''$ . Therefore, the exact width of the extraction used is not highly relevant, but we made it  $2.^{\prime\prime}5$  such that we could

include (properly down-weighted) the full spatial extent of the emission.

### 3. Results

We performed a visual inspection on the reduced 2D and 1D spectra, and found a new Ly $\alpha$  emission line at  $z = 7.60$  from z7\_GND\_16863 (Figure 1(a)), in addition to the visible previously reported Ly $\alpha$  detection at  $z = 7.51$  from z7\_GND\_42912 (Figure 1(b); known as z8\_GND\_5296 in Finkelstein et al. 2013). The other two targets do not have any obvious emission features at the expected slit positions in the 2D spectra. We also ran the automated line search algorithm from Larson et al. (2018), which searches for significant emission features in 1D spectra. Using a threshold of  $5\sigma$  for this automated search, this algorithm finds only these same two reported lines, both at a signal-to-noise ratio (S/N) of  $>10$ .

The Ly $\alpha$  properties for our detected lines are derived from the best-fit asymmetric Gaussian function obtained by running the IDL MPFIT package (Markwardt 2009). The errors of the derived quantities are estimated via Monte-Carlo (MC) simulations by modulating the 1D spectrum with the 1D noise. We perform MC simulations, fitting the asymmetric Gaussian function to the simulated 1D spectra, which are fluctuated by a Gaussian random deviate equal to the associated 1D noise, and we take the standard deviations for the derived Ly $\alpha$  properties from the MC simulation runs.

#### 3.1. z7\_GND\_16863: A New Ly $\alpha$ Detection at $z = 7.60$

As shown in the top row of Figure 1(a) z7\_GND\_16863 is detected only in the NIR HST bands ( $Y_{105}$ ,  $J_{125}$ , and  $H_{160}$ ), and not in the optical bands ( $B_{435}$ ,  $V_{606}$ ,  $i_{775}$ ,  $I_{814}$ , and  $z_{850}$ ), suggesting a strong continuum break; and it is consistent with the expectation of a  $z = 7.60$  galaxy. This object has been targeted in three mask configurations as shown in the bottom right panel of Figure 1(a): GOODSN\_Mask2 (2013 April), GOODSN\_Y\_v12 (2014 March), and Mask2\_Y\_2015A (2015 February) with a total exposure time of  $t_{\text{exp}} = 16.3$  hr. The emission line has been detected at  $10450 \text{ \AA}$  ( $z_{\text{spec}} = 7.60$ ) with an S/N of 10.8. In the 2D spectrum, a strong emission line is shown at the expected slit position with two negative features shown at  $\pm 2.5''$  separations. Interestingly, this spectroscopic redshift deviates from the photometric redshift at the  $\sim 1.5\sigma$  level. Larson et al. (2018) reported a  $2\sigma$  deviation of the photometric redshift from their  $z = 7.452$  galaxy, and photometric redshifts show a substantially higher fraction of catastrophic outliers ( $\Delta z > 0.15$ ) in  $z \sim 6\text{--}7$  (Pentericci et al. 2018), compared to the low- $z$  universe (Dahlen et al. 2013). Along with these recent findings, a statistical number of spectroscopic redshifts is required to precisely calibrate photometric redshifts in the high- $z$  universe at  $z > 7$ .

The strong break between the optical and NIR bands implies that the emission line is either Ly $\alpha$  (if it is the Lyman break) or [O II]  $\lambda\lambda 3726, 3729$  (the rest-frame  $4000 \text{ \AA}$ /Balmer break). We note that other emission lines (e.g., H $\beta$  and [O III]  $\lambda\lambda 4959, 5007$ , or H $\alpha$  with [N II]  $\lambda\lambda 6548, 6584$ ) are additionally ruled out, as the spectral coverage of our observations allows us to detect multiple lines, and we do not see additional lines in the 1D or 2D spectrum. In the case of the [O II] doublet, the MOSFIRE spectral resolution can resolve the doublet with an expected gap of  $\sim 8\text{--}9 \text{ \AA}$  (at  $z = 1.80$ , the redshift if this line was [O II]). Thus, we analyzed the spectrum for signatures of

the other line, but no signal is observed at the expected wavelength. Furthermore, double Gaussian line fitting does not satisfy the theoretical expectation on the [O II] doublet flux ratio of 0.35–1.5 (Pradhan et al. 2006). This low- $z$  solution is also disfavored by galaxy SED fitting with a much larger  $\chi^2$  ( $=23.4$ ) than that of the high- $z$  solution ( $\chi^2 = 2.4$ ) (Figure 2; details described in Section 3.4). Finally, the best -fit low- $z$  solution of the object suggests a very dusty but quenched galaxy with a near-zero star formation rate (SFR), inconsistent with strong [O II] emission, which generally implies star formation (although it could also be caused due to active galactic nucleus (AGN) activity).

#### 3.2. z7\_GND\_42912: A Ly $\alpha$ Emitter at $z = 7.51$

Our targets also include z7\_GND\_42912, shown in Figure 1(b), which was first reported in Finkelstein et al. (2013) as a new Ly $\alpha$  emission detection at  $z = 7.51$  with an S/N ratio of 7.8 from  $\sim 6$  hr of MOSFIRE observations in 2013 April. Here we update the measure of the Ly $\alpha$  line profile from the entire MOSFIRE data set from three masks: GOODSN\_Mask1 (2013 April), GOODSN\_Y\_v12 (2014 March), and Mask2\_Y\_2015A (2015 February) with  $t_{\text{exp}} = 16.5$  hr (bottom right in Figure 1(b)). With a  $\sim 3\times$  longer exposure time, we reveal a clear asymmetric line profile with the updated line flux,  $F_{\text{Ly}\alpha} = 1.46 \pm 0.14 \times 10^{-17} \text{ erg s}^{-1} \text{ cm}^{-2}$  (S/N = 10.8).

We note that our Ly $\alpha$  flux measurement from z7\_GND\_42912 is  $\sim 5\times$  greater than that of Finkelstein et al. (2013). Tilvi et al. (2016) published a *HST*/grism observation of z7\_GND\_42912, finding a  $\sim 4$  times higher Ly $\alpha$  flux than that of Finkelstein et al. (2013). Although the origin of the significant discrepancy between *HST*/grism and Keck/MOSFIRE observations was not clearly known at the time, we found that this is mainly due to an unknown flux calibration issue in the Finkelstein et al. (2013) analysis. The c. 2013 version of the MOSFIRE DRP gives different units between the multi-object spectra frames (electrons  $\text{s}^{-1}$ ) and long-slit frames (ADU/coadd), but this difference in data units was not documented in the DRP documentation, thus these images were treated in the same manner as in Finkelstein et al. (2013). By converting between these two image units, we find that the Finkelstein et al. (2013) line flux should be  $4.65\times$  higher, consistent with our updated measurement. Our updated flux with the same data set (GOODSN\_Mask1) is  $F_{\text{Ly}\alpha} = 1.28 \pm 0.13 \times 10^{-17} \text{ erg s}^{-1} \text{ cm}^{-2}$ , now consistent with that of Tilvi et al. (2016). The flux values from the other individual masks are  $1.48$  and  $1.01 \times 10^{-17} \text{ erg s}^{-1} \text{ cm}^{-2}$  with somewhat different line profiles (GOODSN\_Y\_v12 and Mask2\_Y\_2015A, respectively). Thus, our final flux value in Table 2, which is measured from all combined data, is higher than the Tilvi et al. (2016) value. We note that while the significant variation in measured line flux between our three observations could imply a systematic uncertainty in our flux calibration, simulations have predicted that the measured Ly $\alpha$  flux can depend on the observed slit position angle due to the complicated morphology of the Ly $\alpha$  emission (Smith et al. 2019).

Also, it is worth mentioning that our redshift measurement ( $z_{\text{Ly}\alpha} = 7.5056 \pm 0.0007$ ), derived via an asymmetric Gaussian fit, is significantly different than that from Finkelstein et al. (2013),  $z_{\text{Ly}\alpha} = 7.5078 \pm 0.0004$ , which was measured from symmetric Gaussian fitting. That difference mainly comes from the different assumptions about the line profile: symmetric (Finkelstein et al. 2013) versus asymmetric (this study) Gaussians. Our redshift measurement with a symmetric

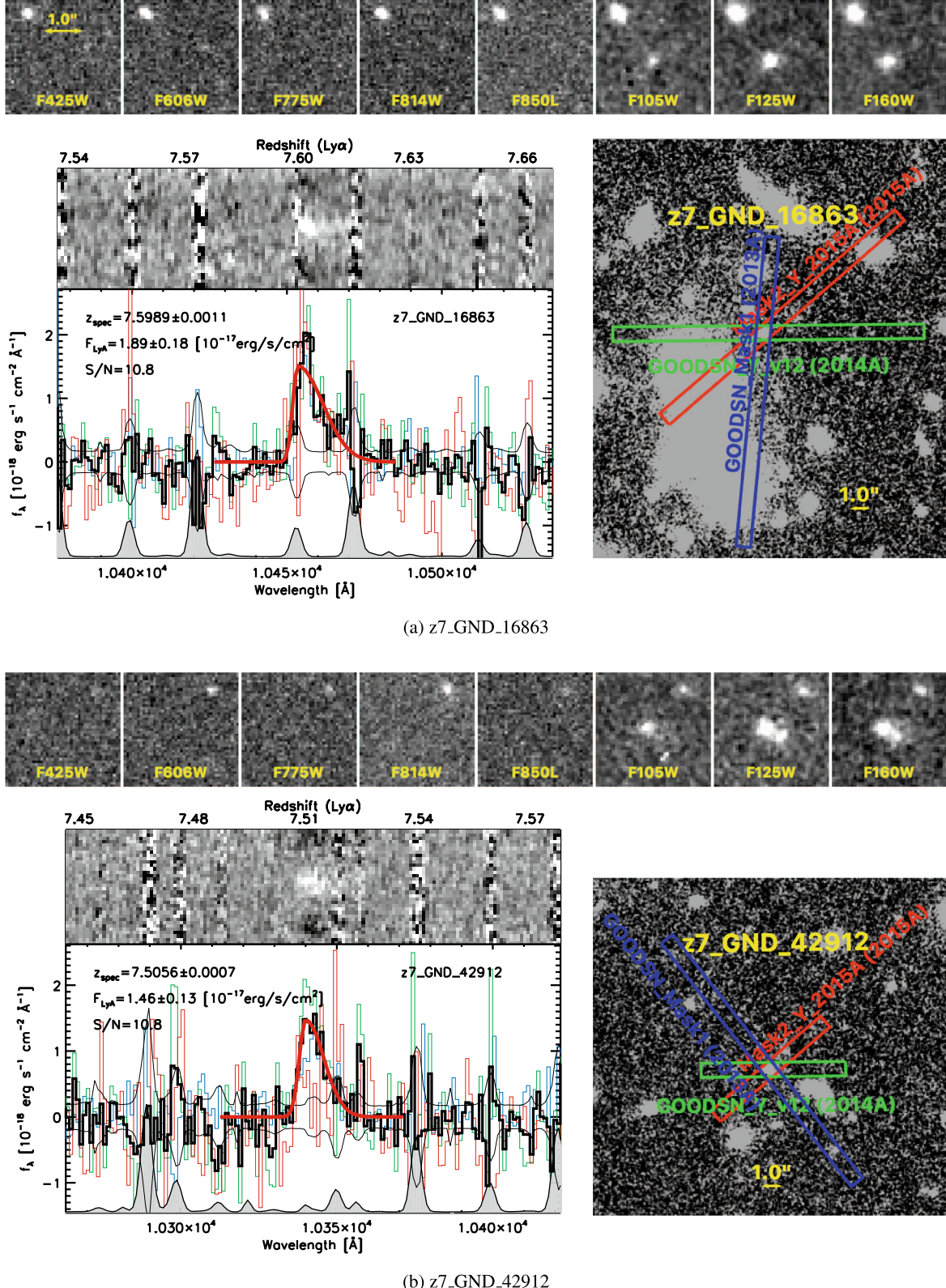
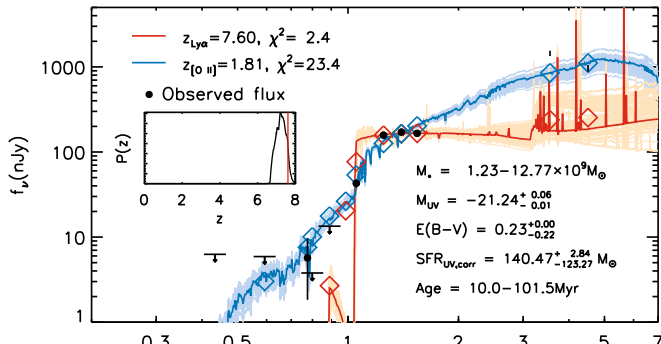
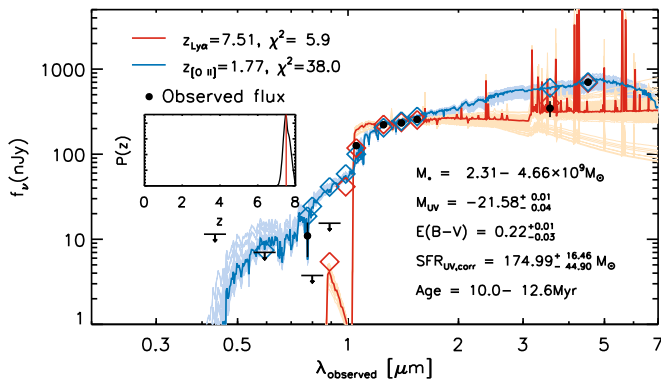


**Figure 1.** (a) *HST* ACS/WFC3 images of  $z7\_GND\_16863$  in the top panel. All images are centered on the object, and the Lyman break is clearly observed between the *HST* optical and NIR filters. The bottom left panel shows the 1D and 2D spectra of  $z7\_GND\_16863$ . In the 2D spectrum, the strong emission line is shown at the expected spatial slit position with the two negative features shown at  $\pm 2''/5$  separation. In the 1D spectrum, the black histogram is the all-mask-combined flux, and the three individual mask fluxes are displayed as colored histograms. The black curves represent the  $1\sigma$  noise level, and the normalized sky emission is plotted at the bottom as a gray filled curve. The red curve is the best-fit asymmetric Gaussian profile. The bottom right panel shows the slit locations of the three observed mask configurations, overlaid on the *HST* WFC3 F160W CANDELS image. The slits are color-coded as histograms in 1D spectra. (b) Same as (a) but for  $z7\_GND\_42912$ .



(a) z7\_GND\_16863



(b) z7\_GND\_42912

**Figure 2.** Galaxy SED fitting results. Each panel shows two SEDs for high- $z$  (Ly $\alpha$ ) and low- $z$  ([O II]) solutions (red and blue solid curves, respectively), and the colored diamond symbols represent continuum fluxes from the model SEDs. The black dots are the observed fluxes with their associated errors, and the downward arrows are  $1\sigma$  upper limits. The physical quantities written in the panels are estimated from the high- $z$  solutions. For the stellar masses and ages, we display the 68% confidence ranges. The insets display photometric redshift probability distributions,  $P(z)$ , taken from S. Finkelstein et al. (2019, in preparation), and the spectroscopic redshifts are shown with vertical red lines.

Gaussian fit provides  $z_{\text{Ly}\alpha} = 7.5072 \pm 0.0003$ , which is more comparable to Finkelstein et al. (2013). As our analysis reveals a significant asymmetric line shape of Ly $\alpha$  emission (which will be discussed in Section 3.3), it is crucial to understand the systematic of the redshift measurement due to the assumptions about the Ly $\alpha$  line profile.

### 3.3. Ly $\alpha$ Emission Properties

The measured emission-line properties of the two Ly $\alpha$  emitting galaxies are listed in Table 3. From z7\_GND\_16863, the Ly $\alpha$  emission line has been detected with  $F_{\text{Ly}\alpha} = 1.89 \pm 0.18 \times 10^{-17} \text{ erg s}^{-1} \text{ cm}^{-2}$  ( $\text{S/N} = 10.8$ ). Although the noise level is very high at the blue side of the line profile due to the nearby sky emission line, the asymmetric feature is still significant, with a  $1\sigma$  lower limit on  $\sigma_{\text{red}}/\sigma_{\text{blue}} > 4.29$ . Our new observations of the Ly $\alpha$  emission line from z7\_GND\_42912 now reveal a significant asymmetric profile of  $\sigma_{\text{red}}/\sigma_{\text{blue}} = 2.98^{+1.64}_{-1.11}$ . This significant asymmetry was not found by Finkelstein et al. (2013), but is revealed in our higher fidelity spectrum. We also calculate the skewness of the Ly $\alpha$  emission-line profiles, which also suggests significant

**Table 3**  
Summary of Emission-line Properties

	z7_GND_16863	z7_GND_42912
$F_{\text{Ly}\alpha} (10^{-17} \text{ erg s}^{-1} \text{ cm}^{-2})$	$1.89 \pm 0.18$	$1.46 \pm 0.14$
Signal-to-noise Ratio	10.79	10.81
$\text{EW}_{\text{Ly}\alpha} (\text{\AA})$	$61.28 \pm 5.85$	$33.19 \pm 3.20$
$z_{\text{Ly}\alpha}$	$7.5989 \pm 0.0011$	$7.5056 \pm 0.0007$
$\sigma_{\text{blue}} (\text{\AA})$	$0.20^{+1.09}_{-0.20}$	$1.39^{+0.42}_{-0.35}$
$\sigma_{\text{red}} (\text{\AA})$	$6.25^{+1.29}_{-1.05}$	$4.11^{+1.00}_{-0.91}$
$\sigma_{\text{red}}/\sigma_{\text{blue}}$	$>4.29^{\text{a}}$	$2.98^{+1.64}_{-1.11}$
$\text{FWHM}_{\text{red}} (\text{\AA})^{\text{b}}$	$14.71^{+3.03}_{-2.46}$	$9.68^{+2.36}_{-2.15}$

#### Notes.

<sup>a</sup>  $1\sigma$  lower limit.

<sup>b</sup> FWHM of the red side of the line ( $2.355\sigma_{\text{red}}$ ).

asymmetry on both emission lines, with  $1.37 \pm 0.23$  (z7\_GND\_16863) and  $1.69 \pm 0.20$  (z7\_GND\_42912).

Estimating Ly $\alpha$  asymmetry, Rhoads et al. (2003) introduced the parameters  $a_f$  and  $a_\lambda$ , which represent the relative flux ratio between the blue and red sides of Ly $\alpha$  emission and the relative peak location from the blue and red ends of the line profile. Dawson et al. (2007) performed a statistical study of  $a_f$  and  $a_\lambda$  with 59 Ly $\alpha$  emitting galaxies, reporting significant asymmetric Ly $\alpha$  emission profiles at  $z \sim 4$ . We also estimate  $a_f$  and  $a_\lambda$  of our Ly $\alpha$  emission lines with  $a_f > 3.70$  and  $a_\lambda > 3.43$  for z7\_GND\_16863 and  $a_f > 1.77$  and  $a_\lambda > 1.67$  ( $1\sigma$  lower limits), further proving their asymmetry. Furthermore, more recent Ly $\alpha$  surveys investigated Ly $\alpha$  profiles, finding significant asymmetry of Ly $\alpha$  emission lines at  $4 < z < 7$  (Hu et al. 2010; Ouchi et al. 2010; Kashikawa et al. 2011; Mallery et al. 2012; U et al. 2015). However, not many high- $z$  Ly $\alpha$  emission lines have reported a significant asymmetric Ly $\alpha$  line profile at  $z > 7$ , presumably due to low S/N, though we note the stacked analysis of Ly $\alpha$  emission shows a clear asymmetric line profile in Pentericci et al. (2018). In addition to Song et al. (2016), which captured the first notable asymmetric line profile with deep NIR spectroscopy with 10 hr of integration time, our analysis of a Ly $\alpha$  line profile with the extremely deep spectroscopy uncovers the asymmetric nature of our two Ly $\alpha$  emission lines at  $z > 7$ .

The asymmetric feature of Ly $\alpha$  emission from high- $z$  galaxies is theoretically expected to be due to absorption by the interstellar medium (ISM) and IGM. Interaction with an outflowing ISM provides easier escape routes for the red wing of Ly $\alpha$  (e.g., Ahn et al. 2001; Dijkstra 2014), thus the redshifted asymmetric Ly $\alpha$  emission-line profile is often explained by common galactic outflows (e.g., Verhamme et al. 2006; Gronke et al. 2015; Remolina-Gutiérrez & Forero-Romero 2019), which could be boosted by cosmic-ray (Gronke et al. 2018) and Ly $\alpha$  feedback (Smith et al. 2017; Kimm et al. 2018). Importantly, recent studies on Ly $\alpha$  profiles with green peas, a local analog of high- $z$  LAEs, have revealed more complex processes related to their Ly $\alpha$  profiles (e.g., Yang et al. 2016, 2017a, 2017b; Orlitová et al. 2018; Verhamme et al. 2018). Therefore, further studies on Ly $\alpha$  profiles are required to illustrate the detailed Ly $\alpha$  radiative processes in ISM.

To place Ly $\alpha$  detection limits for our non-detections, we calculate  $5\sigma$  detection limits of Ly $\alpha$  emission lines in the MOSFIRE Y-band wavelength coverage from  $\sim 9800$  to  $11200 \text{ \AA}$  by adding mock 1D Ly $\alpha$  emission lines to the actual

1D spectra. For simulating the mock Ly $\alpha$  emission lines, we renormalize the best-fit asymmetric Gaussian profile from the detected Ly $\alpha$  emission in z7\_GND\_42912. The measured median  $5\sigma$  detection limit of Ly $\alpha$  emission is down to  $\sim 4 \times 10^{-18}$  erg s $^{-1}$  cm $^{-2}$  between sky lines. This measurement is consistent with the previous observations (e.g., Wirth et al. 2015; Song et al. 2016) when scaling our detection limit by  $\sqrt{t}$ , where  $t$  is the integration time. Compared to the emission-line sensitivity in the MOSDEF survey (Kriek et al. 2015), our Ly $\alpha$  sensitivity is lower by up to a factor of two (for an optimistic case of MOSDEF). The difference is understandable, as MOSDEF has overall better seeing than our data, and the Ly $\alpha$  line profile is generally broader than other emission lines, making it more difficult to detect.

We measure the rest-frame EWs of the detected Ly $\alpha$  lines and place  $5\sigma$  EW upper limits for non-detections. The rest-frame EW is defined as the ratio of the Ly $\alpha$  flux to the UV continuum flux density, divided by  $1+z$ . We derive the UV continuum brightness from the best-fit galaxy SED model (refer to Section 3.4), averaged over the 50 Å window just redward of Ly $\alpha$  emission, from 1230 to 1280 Å. The derived EWs are  $61.28 \pm 5.85$  Å and  $33.19 \pm 3.20$  Å for z7\_GND\_16863 and z7\_GND\_42912, respectively. Previous measures of Ly $\alpha$  EWs in the literature show a deficit of high-EW LAEs ( $>50$  Å) at  $z > 7$  (e.g., Tilvi et al. 2014, and references therein), and the measured EW of the Ly $\alpha$  emission line from z7\_GND\_42912 ( $33.19 \pm 3.20$  Å) is consistent with those measurements. However, the Ly $\alpha$  EW from the new Ly $\alpha$  emission line in z7\_GND\_16863 ( $61.28 \pm 5.85$  Å) is relatively high. Along with the recent observations of Hu et al. (2017), Zheng et al. (2017), and Pentericci et al. (2018), which found high-EW LAEs at  $z \sim 7$ , and Larson et al. (2018), which reported a high-EW object ( $140.3 \pm 19.0$  Å) at  $z \sim 7.5$ , our results suggest that high-EW Ly $\alpha$  emission is not uncommon at  $z > 7$ , although this needs further verification in a future study. We note that we do not detect Ly $\alpha$  emission from z7\_GND\_18869 and z7\_GND\_9408, relatively fainter objects, even with our very deep NIR observations with the  $5\sigma$  EW upper limits of  $<19$  and  $<67$  Å, respectively.

The MOSFIRE Y-band covers the wavelength ranges of N V emission lines, an indicator of AGNs activity, for our two LAEs. For z7\_GND\_16863, we search within 500 km s $^{-1}$  from the expected wavelength (e.g., Steidel et al. 2010; Erb et al. 2014; Stark et al. 2017; Mainali et al. 2018), finding no significant detection, and a  $1\sigma$  upper limit on the N V emission-line flux of  $\lesssim 8.54 \times 10^{-19}$  erg s $^{-1}$  cm $^{-2}$ , corresponding to the Ly $\alpha$ /N V flux ratio  $\gtrsim 22$ . For z7\_GND\_42912, T. Hutchison et al. (2019, in preparation) detected one of the C III] lines with MOSFIRE H-band observations, measuring the systematic redshift to be  $z = 7.5032 \pm 0.0003$  and  $7.4941 \pm 0.0003$ , if their detected lines are C III]  $\lambda 1907$  and C III]  $\lambda 1909$ , respectively. We do not see significant emission for N V at the wavelengths corresponding to these systemic redshifts, and we measure  $1\sigma$  upper limits of  $<7.66$  and  $<6.60 \times 10^{-19}$  erg s $^{-1}$  cm $^{-2}$  at 10543 and 10532 Å, corresponding to Ly $\alpha$ /N V flux ratios of  $>19$  and  $>22$ , respectively. Tilvi et al. (2016) measured a possible detection of N V from z7\_GND\_42912 at  $\lambda \sim 10550$  Å with a slight spatial offset of  $\sim 0.^{\prime\prime}1$  from HST/grism observations, with a reported N V line flux of  $f_{\text{line}} = 0.91 \pm 0.21 \times 10^{-17}$  erg s $^{-1}$  cm $^{-2}$ . Our spectrum should have detected this line with S/N > 10. This non-detection implies that the previously reported N V in

Tilvi et al. (2016) may be contamination. The previously reported measures of the Ly $\alpha$ /N V flux ratio from several  $z \gtrsim 7$  galaxies range from  $\sim 1\text{--}2$  (Hu et al. 2017; Sobral et al. 2017) to  $\sim 6\text{--}9$  (Laporte et al. 2017; Mainali et al. 2018). With the limits of the Ly $\alpha$ /N V flux ratio  $\gtrsim 19\text{--}22$  in our observations, our two LAEs likely do not host significant AGN activity (see also discussion in Castellano et al. 2018).

### 3.4. Physical Properties of $z \sim 7.5$ Galaxies

To derive the physical quantities of our detected galaxies, we perform galaxy SED fitting with stellar population synthesis models (Bruzual & Charlot 2003). The parameter settings, nebular emission lines (Inoue 2011; Salmon et al. 2015), and IGM attenuation (Madau 1995) descriptions in SED fitting are similar to those used in Jung et al. (2017). We take a Salpeter (1955) initial mass function with lower and upper stellar-mass limits of  $0.1\text{--}100 M_{\odot}$ , respectively, and metallicities ranging from 0.005 to  $1.0 Z_{\odot}$ . We allow several star formation histories (SFHs), using a range of exponential models: decrease, increase, and constant SFHs with exponential-decaying time ( $\tau = 10, 100, -300$  Myr, 1, 10, 100,  $-1, -10$  Gyr). Dust attenuation to our model spectra uses the attenuation curve of Calzetti (2001), with  $E(B-V)$  values spanning 0–0.8. We restrict stellar population ages to  $>10$  Myr, to avoid a scenario where a galaxy forms all of its mass in an unphysically small amount of time.

Constraining the stellar mass for high- $z$  galaxies is critically dependent on long-wavelength *Spitzer*/IRAC photometry. However, z7\_GND\_16863 is found in the vicinity of a bright nearby source (Figure 1(a)), making it impossible to properly measure its rest-frame optical continuum with the low-spatial-resolution IRAC photometry. Thus, our SED fitting results of z7\_GND\_16863 with only rest-frame UV fluxes have highly correlated physical parameters (e.g., stellar mass, dust extinction, and age). The Ly $\alpha$  contributions to continuum fluxes were removed during the SED fitting, and we also ignored  $Y_{105}$  fluxes, as it is often difficult to model due to the uncertainty of IGM attenuation. To calculate SFRs, we first obtained dust-corrected UV fluxes from the best-fit models and converted the UV fluxes to SFRs by adopting the updated FUV-to-SFR conversion factor of  $\kappa = 1.15 \times 10^{-28} M_{\odot} \text{ yr}^{-1} \text{ erg}^{-1} \text{ s Hz}$  (Madau & Dickinson 2014). This is derived from the stellar population models of Conroy et al. (2009) and is  $\sim 20\%$  lower than the conventional conversion factor in Kennicutt (1998). This is also similar to the other recent studies (e.g., Salim et al. 2007; Haardt & Madau 2012) based on Bruzual & Charlot (2003), which found lower mean conversion factors.

Figure 2 shows our SED fitting results for z7\_GND\_16863 (top) and z7\_GND\_42912 (bottom). The best-fit model is chosen by minimizing  $\chi^2$ . The fitting errors are obtained via MC simulations. We run 1000 MC simulations to derive the best-fit models with the simulated continuum fluxes. In the MC simulations, we fluctuate the observed fluxes with Gaussian random deviates, which are equivalent to the flux measurement errors to simulate the continuum fluxes, and we perform SED fitting with the simulated fluxes.

z7\_GND\_16863 and z7\_GND\_42912 are very bright in the rest-frame UV ( $M_{\text{UV}} = -21.24$  and  $-21.58$ , respectively), relative to the characteristic UV magnitudes of  $z \sim 7\text{--}8$  galaxies of  $M_{\text{UV}} \sim 21$  (Finkelstein et al. 2015). The stellar masses of the two objects are consistent with that expected

from the published scaling relation between  $M_*$  and  $M_{\text{UV}}$  at  $z > 7$  (Song et al. 2016), although the stellar mass of z7\_GND\_16863 is not well-constrained due to the lack of the rest-frame optical photometric constraints. The two Ly $\alpha$  emitters are actively forming stars with SFRs [ $M_{\odot} \text{ yr}^{-1}$ ] =  $140^{+3}_{-123}$  (z7\_GND\_16863) and  $175^{+16}_{-45}$  (z7\_GND\_42912). These SFRs are above the fiducial  $M_*$ –SFR relation of high- $z$  galaxies (e.g., Salmon et al. 2015; Song et al. 2016; Jung et al. 2017), which suggests  $\sim 10\text{--}30 M_{\odot} \text{ yr}^{-1}$  for  $\sim 10^{9\text{--}10} M_{\odot}$  galaxies at  $z \sim 6$ , although this relation likely increases at higher redshift. Particularly, our updated measurement of z7\_GND\_42912 with young stellar populations (age  $< 12.6$  Myr) and a high SFR is comparable to but less extreme than Finkelstein et al. (2013), which found the time-averaged SFR of z7\_GND\_42912 to higher than  $330 M_{\odot} \text{ yr}^{-1}$  with extremely young stellar populations (age  $\sim 1\text{--}3$  Myr [1 $\sigma$ ], which is less than we allowed in our model fitting). We also calculate time-averaged SFRs by simply dividing the stellar mass by the stellar population age. The averaged SFRs of the galaxies are  $\gtrsim 85$  and  $\gtrsim 216 M_{\odot} \text{ yr}^{-1}$  in their 1 $\sigma$  low limits for z7\_GND\_16863 and z7\_GND\_42912, respectively. Even with their large uncertainties, our  $z \sim 7.5$  Ly $\alpha$  emitting galaxies require high SFRs to build up their stellar masses. Such high SFRs are expected to produce their asymmetric Ly $\alpha$  profiles with strong galactic outflows due to stellar feedback.

#### 4. Summary and Discussion

We analyze our deepest NIR spectroscopic observations with Keck/MOSFIRE for four target galaxies at  $z_{\text{phot}} \gtrsim 7$  with  $\gtrsim 16$  hr of integration time. We detect two Ly $\alpha$  emission lines from UV-bright and actively star-forming galaxies, discovering a new Ly $\alpha$  emitting system at  $z = 7.60$  (z7\_GND\_16863), as well as providing an updated measure of a  $z = 7.51$  Ly $\alpha$  emission line (z7\_GND\_42912) that was previously reported in Finkelstein et al. (2013) and Tilvi et al. (2016). We measure the detailed Ly $\alpha$  line profiles, finding significant Ly $\alpha$  asymmetry. The detection of Ly $\alpha$  from two out of three bright sources ( $M_{\text{UV}} < -20.25$ ) could imply that these bright galaxies inhabit ionized bubbles in a partially neutral IGM, although deeper exposures may yet reveal Ly $\alpha$  emission in the fainter source.

With the current consensus from Ly $\alpha$  studies around the end of reionization at  $z \sim 6\text{--}7$ , Ly $\alpha$  visibility is expected to decrease as the IGM becomes neutral into the epoch of reionization, and it is also expected to have a significant dependence on the UV brightness of galaxies. Conventionally, galaxies are divided into bright ( $M_{\text{UV}} < -20.25$ ) and faint ( $M_{\text{UV}} > -20.25$ ) groups, and the Ly $\alpha$  fraction from faint sources is observationally suggested to be higher than that from bright ones (e.g., Stark 2016, and references therein). Particularly, Pentericci et al. (2018) found a higher Ly $\alpha$  fraction among faint samples again at  $z \sim 7$ . This is explained by bright galaxies more likely being more evolved, with a higher metallicity and larger amount of dust, reducing the Ly $\alpha$  photon escape probability.

On the contrary, many recent results at  $z > 7$  (Oesch et al. 2015; Zitrin et al. 2015; Roberts-Borsani et al. 2016; Stark et al. 2017; Hashimoto et al. 2018) suggest that very bright galaxies reside in ionized bubbles, allowing a larger transmission of Ly $\alpha$  emission than faint sources. Similarly, Castellano et al. (2018) found more Ly $\alpha$  detections than expected among bright galaxies, while they failed to find faint galaxies that emit Ly $\alpha$  photons at  $z \sim 7$ . One possible explanation is that brighter

galaxies reside in early overdensities, which are ionized earlier compared to the rest of the universe. In addition, as discussed in Mason et al. (2018), Ly $\alpha$  photons from bright sources could escape more easily due to their higher velocity offsets from the systemic redshifts, making them less affected by neutral hydrogen in the IGM.

Furthermore, Zheng et al. (2017) reported a “bump” at the bright end of the Ly $\alpha$  LF at  $z \sim 7$  from the Lyman Alpha Galaxies in the Epoch of Reionization survey, indicative of large ionized bubbles where we could see different evolution at the bright and faint ends of the Ly $\alpha$  LF. In the same context, our two detected Ly $\alpha$  emission lines from three bright sources ( $M_{\text{UV}} < -20.25$ ) suggest that the Ly $\alpha$  visibility of UV-bright galaxies does not decrease as much as that of faint galaxies at  $z > 7$ . Of course, this is highly tentative, as the number of targets in our study is small, and we require observations for fainter objects deeper than those for the bright ones to achieve comparable Ly $\alpha$  EW detection limits. Therefore, a comprehensive analysis is necessary to ensure that the Ly $\alpha$  detection rate is higher among brighter galaxies at  $z > 7$ .

Our entire MOSFIRE data set will be included in a future publication in which we will place a strong constraint on the Ly $\alpha$  visibility into  $z > 7$  with a more comprehensive data set of NIR spectroscopic follow-up observations. Furthermore, Ly $\alpha$  studies in the even earlier universe are promising with *James Webb Space Telescope* NIR spectroscopy (Smith et al. 2019), and a future Ly $\alpha$  survey project with the extremely large telescopes (e.g., the Giant Magellan Telescope) will deliver an extensive Ly $\alpha$  data set, allowing us to explore large areas and study the topology of reionization.

The authors wish to acknowledge the very significant cultural role and reverence that the summit of Maunakea has always had within the indigenous Hawaiian community. We are most fortunate to have the opportunity to conduct our observations from this mountain. I.J. acknowledges support from the NASA Headquarters under the NASA Earth and Space Science Fellowship Program—Grant 80NSSC17K0532. I.J. and S.F. acknowledge support from NSF AAG award AST-1518183.

#### ORCID iDs

- Intae Jung  <https://orcid.org/0000-0003-1187-4240>
- Steven L. Finkelstein  <https://orcid.org/0000-0001-8519-1130>
- Taylor A. Hutchison  <https://orcid.org/0000-0001-6251-4988>
- Rebecca L. Larson  <https://orcid.org/0000-0003-2366-8858>
- Casey Papovich  <https://orcid.org/0000-0001-7503-8482>
- Laura Pentericci  <https://orcid.org/0000-0001-8940-6768>
- Mimi Song  <https://orcid.org/0000-0002-8442-3128>
- Henry C. Ferguson  <https://orcid.org/0000-0001-7113-2738>
- Sangeeta Malhotra  <https://orcid.org/0000-0002-9226-5350>
- James Rhoads  <https://orcid.org/0000-0002-1501-454X>
- Vithal Tilvi  <https://orcid.org/0000-0001-8514-7105>
- Isak Wold  <https://orcid.org/0000-0002-0784-1852>

#### References

- Ahn, S.-H., Lee, H.-W., & Lee, H. M. 2001, *ApJ*, 554, 604
- Appenzeller, I. (ed.) 2013, Introduction to Astronomical Spectroscopy (Cambridge: Cambridge Univ. Press)
- Becker, G. D., Davies, F. B., Furlanetto, S. R., et al. 2018, *ApJ*, 863, 92

- Becker, R. H., Fan, X., White, R. L., et al. 2001, *AJ*, **122**, 2850  
 Bolton, J. S., Haehnelt, M. G., Warren, S. J., et al. 2011, *MNRAS*, **416**, L70  
 Bosman, S. E. I., Fan, X., Jiang, L., et al. 2018, *MNRAS*, **479**, 1055  
 Bruzual, G., & Charlot, S. 2003, *MNRAS*, **344**, 1000  
 Calzetti, D. 2001, *New Astron.*, **45**, 601  
 Caruana, J., Bunker, A. J., Wilkins, S. M., et al. 2012, *MNRAS*, **427**, 3055  
 Caruana, J., Bunker, A. J., Wilkins, S. M., et al. 2014, *MNRAS*, **443**, 2831  
 Castellano, M., Pentericci, L., Vanzella, E., et al. 2018, *ApJL*, **863**, L3  
 Conroy, C., Gunn, J. E., & White, M. 2009, *ApJ*, **699**, 486  
 Curtis-Lake, E., McLure, R. J., Pearce, H. J., et al. 2012, *MNRAS*, **422**, 1425  
 Dahlen, T., Mobasher, B., Faber, S. M., et al. 2013, *ApJ*, **775**, 93  
 Dawson, S., Rhoads, J. E., Malhotra, S., et al. 2007, *ApJ*, **671**, 1227  
 Dayal, P., Maselli, A., & Ferrara, A. 2011, *MNRAS*, **410**, 830  
 Dijkstra, M. 2014, *PASA*, **31**, e040  
 Erb, D. K., Steidel, C. C., Trainor, R. F., et al. 2014, *ApJ*, **795**, 33  
 Fan, X., Strauss, M. A., Becker, R. H., et al. 2006, *AJ*, **132**, 117  
 Finkelstein, S. L., Papovich, C., Dickinson, M., et al. 2013, *Natur*, **502**, 524  
 Finkelstein, S. L., Ryan, R. E., Jr., Papovich, C., et al. 2015, *ApJ*, **810**, 71  
 Fontana, A., Vanzella, E., Pentericci, L., et al. 2010, *ApJL*, **725**, L205  
 Gronke, M., Bull, P., & Dijkstra, M. 2015, *ApJ*, **812**, 123  
 Gronke, M., Girichidis, P., Naab, T., & Walch, S. 2018, *ApJL*, **862**, L7  
 Haardt, F., & Madau, P. 2012, *ApJ*, **746**, 125  
 Hashimoto, T., Laporte, N., Mawatari, K., et al. 2018, *Natur*, **557**, 392  
 Hoag, A., Bradač, M., Trenti, M., et al. 2017, *NatAs*, **1**, 0091  
 Horne, K. 1986, *PASP*, **98**, 609  
 Hu, E. M., Cowie, L. L., Barger, A. J., et al. 2010, *ApJ*, **725**, 394  
 Hu, W., Wang, J., Zheng, Z.-Y., et al. 2017, *ApJL*, **845**, L16  
 Inoue, A. K. 2011, *MNRAS*, **415**, 2920  
 Jung, I., Finkelstein, S. L., Livermore, R. C., et al. 2018, *ApJ*, **864**, 103  
 Jung, I., Finkelstein, S. L., Song, M., et al. 2017, *ApJ*, **834**, 81  
 Kashikawa, N., Shimasaku, K., Matsuda, Y., et al. 2011, *ApJ*, **734**, 119  
 Kennicutt, R. C., Jr. 1998, *ARA&A*, **36**, 189  
 Kimm, T., Haehnelt, M., Blaizot, J., et al. 2018, *MNRAS*, **475**, 4617  
 Konno, A., Ouchi, M., Shibuya, T., et al. 2018, *PASJ*, **70**, S16  
 Kriek, M., Shapley, A. E., Reddy, N. A., et al. 2015, *ApJS*, **218**, 15  
 Kurucz, R. L. 1993, SYNTHE spectrum synthesis programs and line data CD-ROM (Cambridge, MA: Smithsonian Astrophysical Observatory)  
 Laporte, N., Ellis, R. S., Boone, F., et al. 2017, *ApJL*, **837**, L21  
 Laporte, N., Nakajima, K., Ellis, R. S., et al. 2017, *ApJ*, **851**, 40  
 Larson, D., Dunkley, J., Hinshaw, G., et al. 2011, *ApJS*, **192**, 16  
 Larson, R. L., Finkelstein, S. L., Pirzkal, N., et al. 2018, *ApJ*, **858**, 94  
 Madau, P. 1995, *ApJ*, **441**, 18  
 Madau, P., & Dickinson, M. 2014, *ARA&A*, **52**, 415  
 Mainali, R., Zitrin, A., Stark, D. P., et al. 2018, *MNRAS*, **479**, 1180  
 Malhotra, S., & Rhoads, J. E. 2004, *ApJL*, **617**, L5  
 Mallery, R. P., Mobasher, B., Capak, P., et al. 2012, *ApJ*, **760**, 128  
 Markwardt, C. B. 2009, *adass XVIII*, **411**, 251  
 Mason, C. A., Treu, T., de Barros, S., et al. 2018, *ApJL*, **857**, L11  
 McGreer, I. D., Mesinger, A., & D'Odorico, V. 2015, *MNRAS*, **447**, 499  
 Miralda-Escudé, J., & Rees, M. J. 1998, *ApJ*, **497**, 21  
 Mortlock, D. J., Warren, S. J., Venemans, B. P., et al. 2011, *Natur*, **474**, 616  
 Oesch, P. A., van Dokkum, P. G., Illingworth, G. D., et al. 2015, *ApJL*, **804**, L30  
 Oke, J. B., & Gunn, J. E. 1983, *ApJ*, **266**, 713  
 Ono, Y., Ouchi, M., Mobasher, B., et al. 2012, *ApJ*, **744**, 83  
 Orlitová, I., Verhamme, A., Henry, A., et al. 2018, *A&A*, **616**, A60  
 Ouchi, M., Shimasaku, K., Furusawa, H., et al. 2010, *ApJ*, **723**, 869  
 Pentericci, L., Fontana, A., Vanzella, E., et al. 2011, *ApJ*, **743**, 132  
 Pentericci, L., Vanzella, E., Castellano, M., et al. 2018, *A&A*, **619**, A147  
 Pentericci, L., Vanzella, E., Fontana, A., et al. 2014, *ApJ*, **793**, 113  
 Planck Collaboration, Ade, P. A. R., Aghanim, N., et al. 2016, *A&A*, **594**, A13  
 Pradhan, A. K., Montenegro, M., Nahar, S. N., & Eissner, W. 2006, *MNRAS*, **366**, L6  
 Remolina-Gutiérrez, M. C., & Forero-Romero, J. E. 2019, *MNRAS*, **482**, 4553  
 Rhoads, J. E., Dey, A., Malhotra, S., et al. 2003, *AJ*, **125**, 1006  
 Rhoads, J. E., & Malhotra, S. 2001, *ApJL*, **563**, L5  
 Roberts-Borsani, G. W., Bouwens, R. J., Oesch, P. A., et al. 2016, *ApJ*, **823**, 143  
 Robertson, B. E., Ellis, R. S., Furlanetto, S. R., & Dunlop, J. S. 2015, *ApJL*, **802**, L19  
 Rybicki, G. B., & Loeb, A. 1999, *ApJL*, **520**, L79  
 Salim, S., Rich, R. M., Charlot, S., et al. 2007, *ApJS*, **173**, 267  
 Salmon, B., Papovich, C., Finkelstein, S. L., et al. 2015, *ApJ*, **799**, 183  
 Salpeter, E. E. 1955, *ApJ*, **121**, 161  
 Santos, M. R. 2004, *MNRAS*, **349**, 1137  
 Schenker, M. A., Ellis, R. S., Konidaris, N. P., & Stark, D. P. 2014, *ApJ*, **795**, 20  
 Schenker, M. A., Stark, D. P., Ellis, R. S., et al. 2012, *ApJ*, **744**, 179  
 Schmidt, K. B., Treu, T., Bradač, M., et al. 2016, *ApJ*, **818**, 38  
 Shibuya, T., Kashikawa, N., Ota, K., et al. 2012, *ApJ*, **752**, 114  
 Smith, A., Bromm, V., & Loeb, A. 2017, *MNRAS*, **464**, 2963  
 Smith, A., Ma, X., Bromm, V., et al. 2019, *MNRAS*, **484**, 39  
 Sobral, D., Matthee, J., Best, P., et al. 2017, *MNRAS*, **466**, 1242  
 Song, M., Finkelstein, S. L., Ashby, M. L. N., et al. 2016, *ApJ*, **825**, 5  
 Song, M., Finkelstein, S. L., Livermore, R. C., et al. 2016, *ApJ*, **826**, 113  
 Stark, D. P. 2016, *ARA&A*, **54**, 761  
 Stark, D. P., Ellis, R. S., Charlot, S., et al. 2017, *MNRAS*, **464**, 469  
 Stark, D. P., Ellis, R. S., Chiu, K., Ouchi, M., & Bunker, A. 2010, *MNRAS*, **408**, 1628  
 Steidel, C. C., Erb, D. K., Shapley, A. E., et al. 2010, *ApJ*, **717**, 289  
 Tilvi, V., Papovich, C., Finkelstein, S. L., et al. 2014, *ApJ*, **794**, 5  
 Tilvi, V., Pirzkal, N., Malhotra, S., et al. 2016, *ApJL*, **827**, L14  
 Treu, T., Schmidt, K. B., Trenti, M., Bradley, L. D., & Stiavelli, M. 2013, *ApJL*, **775**, L29  
 Treu, T., Trenti, M., Stiavelli, M., Auger, M. W., & Bradley, L. D. 2012, *ApJ*, **747**, 27  
 U, V., Hemmati, S., Darvish, B., et al. 2015, *ApJ*, **815**, 57  
 van Leeuwen, F. 2007, *A&A*, **474**, 653  
 Vanzella, E., Fontana, A., Pentericci, L., et al. 2014, *A&A*, **569**, A78  
 Verhamme, A., Garel, T., Ventou, E., et al. 2018, *MNRAS*, **478**, L60  
 Verhamme, A., Schaerer, D., & Maselli, A. 2006, *A&A*, **460**, 397  
 Wirth, G. D., Trump, J. R., Barro, G., et al. 2015, *AJ*, **150**, 153  
 Yang, H., Malhotra, S., Gronke, M., et al. 2016, *ApJ*, **820**, 130  
 Yang, H., Malhotra, S., Gronke, M., et al. 2017a, *ApJ*, **844**, 171  
 Yang, H., Malhotra, S., Rhoads, J. E., et al. 2017b, *ApJ*, **838**, 4  
 Zheng, Z.-Y., Wang, J., Rhoads, J., et al. 2017, *ApJL*, **842**, L22  
 Zitrin, A., Labb  , I., Belli, S., et al. 2015, *ApJL*, **810**, L12